Hydrodynamics at a microtidal inlet: Analysis of propagation of the main wave components

Hydrodynamics at a Microtidal Inlet: Analysis of Propagation of the Main Wave Components

Lorenzo Melito[a], Matteo Postacchini[a], Alex Sheremet[b], Joseph Calantoni[c], Gianluca Zitti[a], Giovanna Darvini[a], Pierluigi Penna[d], Maurizio Brocchini[a]

[a]*Department of Ingegneria Civile, Edile e Architettura, Università Politecnica delle Marche, Ancona, Italy*

[b]*University of Florida, Gainesville, FL, USA*

[c]*Marine Geosciences Division, U.S. Naval Research Laboratory, Stennis Space Center, MS, USA*

[d]*National Research Council CNR IRBIM, Ancona, Italy*

Abstract

The evolution of different wave components as they propagate within a microtidal inlet during a storm occurring from 24–26 January 2014 is analyzed, in order to improve knowledge on how microtidal river mouths typical of the Adriatic Sea behave. For the first time, the "low-pass filter" mechanism previously ascertained at several macrotidal oceanic inlets around the world has been observed in the field with remarkably specific hydrodynamic conditions, i.e. low tide excursion, permanent connection with the sea and generally milder wave climate than in the ocean. Sea/swell (SS) waves were strongly dissipated before entering the river mouth, through the combined action of wave breaking due to reducing depths and opposing river currents enhanced by rainfall. Infragravity (IG) waves propagated upstream and significant IG wave heights of up to 0.4 m, about 13% of the local water depth, have been observed 400 m upriver (about 10 times the local SS peak wavelength) during storm climax. The IG wave energy here represented over 4% of the maximum offshore storm energy. IG wave components travelled upriver at estimated velocities between 3.6 m/s and 5.5 m/s (comparable with speeds of nonlinear long waves) during intense storm stages up to 600 m into the river channel (about 15 times the local SS

Email address: `l.melito@pm.univpm.it` (Lorenzo Melito)

peak wavelength), and are enhanced by tide-induced increase in water depths. It is estimated that tide-induced excursion accounted for about 80% of the total mean water elevation at storm peak at about 400 m into the river. Finally, tidal oscillations are detected up to 1.5 km upstream (about 40 times the local SS peak wavelength). This study highlights the dominance of astronomical tide over both wave setup and storm surge in controlling the upriver propagation of IG waves, even in a microtidal environment.

Keywords: river mouth, estuary, microtidal estuary, wave-current interaction, infragravity waves, storms, calm-storm transition

---

1. Introduction

River mouths are strongly dynamic environments, where a great number of hydrological and morphological processes take place simultaneously and influence each other. The complex nonlinear interactions among bathymetry, waves and currents play a key role in defining the hydro-morphodynamic behaviour of coastal settings like estuaries, deltas and inlets [1, 2, 3, 4]. However, the relevant features of these nonlinear interactions are still ambiguous and need more research to be fully understood.

Much attention over the last decades has been devoted to a better comprehension of infragravity (IG) waves [5]. IG waves are defined as low-frequency ocean surface oscillations with period ranging from 25 seconds to five minutes [6, 7], generated either as group bound long waves [8, 9] or by a temporal variation of the breakpoint [10]. Further, IG waves may also generate from the nonlinear interaction between swell components, then propagate in the surf zone and be refractively trapped on a mildly sloping beach [11]. Such low-frequency oscillations have an important influence on the surf zone hydrodynamics (e.g., see [12, 13, 14, 15, 16, 17, 18, 19] and cited literature therein) and on swash properties, particularly on dissipative beaches [12, 19, 20, 21, 22]. The influence of IG motions in sediment transport processes in the nearshore has been also widely investigated (e.g., see [23, 24, 25, 26, 27] and references therein).

Notwithstanding such interest, the study of IG motions at microtidal estuaries has received comparatively less attention than for other coastal features and structures such as tide-dominated inlets [28, 29], wave-dominated inlets [30], reefs [16, 31], coastal dunes [32] and harbours [33, 34, 35, 36].

Measurements within the small estuary of the Ría de Santiuste (Spain) [37] have revealed a consistent upriver propagation of waves in the IG band (4.3–4.8 minutes) and current velocity amplitudes of up to 0.1 m/s despite the strong discharging flow. Such waves and related currents were amplified as they progressed toward the inner parts of the river, probably due to the effect of edge waves entering the estuary and producing resonance. Field measurement campaigns conducted at the shallow, wave-dominated Albufeira Lagoon inlet (Portugal) [2, 30] have also shown the presence of long period oscillations in water levels in the back-barrier lagoon, due to IG waves developing in the region of the ebb delta. IG wave propagation appears to be tide-modulated; IG waves are the most intense during the flood phase and are blocked during the ebb phase. An extensive analysis of field measurements at the shallow inlet of the Pescadero river, North California [28] have similarly revealed large IG-related oscillations in flow velocity, often of the same order of magnitude of tide-induced currents, as well as upstream-propagating low frequency waves within the estuary. IG velocities appear to have maximum amplitude with high flood velocities, while they are damped during ebb.

Here we present observations of the hydrodynamic phenomena occurring at the microtidal estuary of the Misa River (Senigallia, Italy) in two successive storm events during an experimental campaign performed in January 2014 [38]. A combined analysis of offshore and riverine forcing actions is performed to clarify the processes that either generate or evolve before, during and after storm events, e.g. the evolution, dissipation and relevance of the main wave modes (sea/swell (SS) waves, IG waves, tides) motion and dissipation within the river, and the interactions between sea and river forcings. Additional information from a recently installed hydrometer complement the study by giving insight into the penetration of tidal forcing into the river. The regional setting, the

Figure 1: Study site (images adapted from Google Earth). **a)** Map of Italy and locations of Ancona and Senigallia. **b)** Locations of deployed instrumentation during the field sampling campaign in January 2014. **c)** Locations of hydrometers measuring in February-March 2018.

experimental setup deployed during the original field campaign and the analytical tools adopted in the present study are briefly described in Section 2. Section 3 presents observations on the evolution of wave components and energetic content from offshore to into the river mouth, along with considerations on the interaction between sea and river forcings in different space and time scales. The main findings are discussed in Section 4. Concluding remarks are presented in Section 5.

2. Materials and Methods

2.1. Regional setting and instrumentation

Two field campaigns have been carried out in September 2013, during summertime conditions, and January 2014, in a wintertime regime, in the area around the microtidal estuary (mean tidal range less than 0.6 m) of the Misa River (MR hereinafter), a natural stream located in central Italy and flowing into the Adriatic Sea. The final reach of the river flows within a fixed engineered channel through the town of Senigallia (Marche Region), one of the most important touristic towns of the Italian Middle Adriatic coast (Figure 1a). At the time of the measurements (2013–2014) the river was regularly dredged.

The MR has a total watershed of about 383 km^2 and a river discharge of about 400 m^3/s for a return period of 100 years. Although showing a low flow regime during summer [39], in wintertime the MR features a strongly increased surface flow that dominates over the action of waves and tides.

The MR estuary is classified as a salt-wedge estuary, where freshwater flows out to sea in the upper layer of the water column, while seawater intrusion occurs in the lower layer [40]. Salt water intrusion is confirmed by salinity values larger than 10 psu 700 m upstream of the river mouth, and smaller, although non-zero values up to 1.5 km upstream of the mouth during summer [39]. Small landward velocities in the lower part of the water column (up to 1–1.5 m above the bed) during salt wedge intrusion have been also detected 500 m upstream of the estuary during winter (see the top and center panels of Figure 3 in [38]). As typical for rivers originating in the Apennine Mountains, the MR is also characterized by large sediment transport rates in spite of its moderate discharge. The intense sediment outflow has been postulated to have an influence on the evolution of morphological features of the unprotected beaches southward of the estuary [41].

The two field campaigns have been performed in the context of the EsCoSed project, which aimed at characterizing estuarine morphodynamics in summer and winter conditions as well as their differences [38]. To this purpose, specific equipment was deployed to measure hydrodynamics features in the lower part of the MR and the close nearshore area. The present work largely focuses on the observations from equipment deployed over the wintertime campaign of January 2014. Two quadpods were deployed in the sea at locations QS2 and QS1, at water depths of around 6.5 m and 5.3 m, respectively (Figure 1b). Other quadpods were placed at various locations inside the final reach of the MR at locations QR1, QR2, and QR3 (at 530 m, 400 m and 290 m upstream from the mouth, and located at mean water depths of 2.7, 3.0 and 2.9 m, respectively). A complete description of the instrumental setup can be found in [38]. Two additional tide gauges, TGdown and TGup, were also located in the river at about 280 m and 580 m from the MR mouth, respectively. The locations of the equipment involved in the present study are illustrated in Figure 1b.

To observe the propagation of the sea forcing actions within the MR, additional gauge measurements have been included in this study. Data collected by the river hydrometers installed at "Ponte Garibaldi" ($\sim$ 1.5 km from the MR estuary, RG1 hereafter) and "Bettolelle" ($\sim$ 10 km from the MR estuary, RG2 hereafter; Figure 1c) have been analyzed. The "Ponte Garibaldi" river gauge has been installed in 2016 by the Civil Protection of the Marche Region at a distance of around 1.5 km from the mouth, just upstream of Ponte Garibaldi, a 40 m-long bridge located in the city center. It has been placed in an area along the ending reach of the river where sea intrusion is still detectable [39]. Data from RG1 and RG2 are used in Section 3.6 to discuss some significant flood events in the first few months of 2018, occurred with contextual wave and wind states similar to those observed in January 2014.

The river gauges have a resolution of one datum every 30 min, much lower than that of the majority of the EsCoSed instrumentation (2 Hz). Although SS waves cannot be captured by river gauges, the tidal influence can be easily observed at these locations. Comparisons are shown in Section 3.6 between RG signals and the signal of the tide gauge of the Ancona harbour, located about 30 km south of Senigallia (Figure 1a). The Ancona harbour tide gauge records water level data at a frequency of 0.1 Hz. Preliminary observations on tidal propagation into the MR estuary have been previously presented in [42].

2.2. Methods

In order to evaluate the wave state energetic content in the offshore and into the river estuary, a spectral analysis has been performed. Starting points for the analysis are the water elevation time signals detected by the respective pressure sensors: quadpod QS2 for the analysis of offshore sea state (Section 3.1), and river gauge QR2 for the analysis of wave propagation into the estuary (Section 3.2). For each recording hour, the corresponding wave spectral energy density $\mathcal{E}$ has been determined through a discrete Fourier transform of the hourly de-tided water elevation signals over a frequency domain 0–1.0 Hz. All spectra have been obtained with a number of DOF equal to 41. Once $\mathcal{E}$ is obtained, the energy flux density $\mathcal{F}$ at that hour is $\mathcal{F} = \mathcal{E} c_g$, where c_g is the group velocity. An evaluation of the spectral centroidal frequency f_c of each hourly spectrum is moreover performed as the weighted mean of the frequency range, with the flux density as the weights.

To study the temporal evolution of energy fluxes $\mathcal{F}$ at a specific location, the entire frequency range is divided into three bands representing domains characterized by different physics: the IG band (0.0016–0.05 Hz), the SS band (0.05–0.3 Hz) and the wind waves band (0.3–1 Hz). The band-specific flux Φ_{band} is defined by integrating the flux density $\mathcal{F}$ over each band:

$$\Phi_{\text{band}} = \int_{f_{\text{start}}}^{f_{\text{end}}} \mathcal{F}(f)\ \mathrm{d}f, \tag{1}$$

where f_{start} and f_{end} are the start and end frequencies of each band. Additionally, band-specific significant wave heights H_{sig} have been calculated as $H_{\text{sig}} = 4\sqrt{m_0}$, where m_0 is the 0-th moment of the spectral energy density $\mathcal{E}$ in the specific band.

Section 3.5 gives an analysis of wave energy propagation from the offshore to within the river mouth. To this purpose the wave energy (total, of SS waves or of IG waves) is evaluated as a function of the significant wave height at a specific sensor through the classical relation valid for random gravity waves:

$$E = \frac{\rho g H_{\text{sig}}^2}{16}. \tag{2}$$

Wave energy is also used to evaluate the cross-shore radiation stress, main driver of the wave-induced setup [9, 43]:

$$S_{xx} = E\left(2n - \frac{1}{2}\right), \tag{3}$$

where $n = c_g/c$ is the ratio of group velocity to wave celerity. In the assumption of approaching shallow waters c tends to $\sqrt{gh}$, where h is the water depth. For a given hour, group celerity c_g is evaluated as the mean of the group celerities $c_g(f)$, with $f \in (0\text{–}1.0]$ Hz.

Also in Section 3.5 an evaluation of upriver propagation velocities of IG wave components is attempted. In order to remove the sea and swell wave components from signals, a low-pass filtering (with passband frequency of 0.05 Hz) of the de-tided signals of river sensors has been performed. A cross-correlation of low-frequency signals between consecutive gauges was performed to furnish an estimate for the time t_{lag} it takes for IG wave components to travel from a gauge to another, and therefore give a proxy for the velocity of propagation of IG oscillations:

$$c_{\text{IG}} \approx \frac{\Delta x}{t_{\text{lag}}} \tag{4}$$

where Δx is the distance between two consecutive gauges inside the river. We here stress the fact that, by using Equation (4), we assume that only IG progressive waves are taken into consideration and possible reflected and/or standing waves developing into the channel are therefore not considered.

An IG wave attenuation rate R_{IG} is also used in Section 3.5 to better appraise the decay of low frequency components across the lower reach of the MR:

$$R_{\text{IG}} = \frac{H_{\text{sig,IG,TGdown}} - H_{\text{sig,IG,TGup}}}{H_{\text{sig,IG,TGdown}}} \cdot 100, \tag{5}$$

where $H_{\text{sig,IG,TGdown}}$ and $H_{\text{sig,IG,TGup}}$ are the significant heights of IG components at sensors TGdown and TGup, respectively.

Finally, in Section 3.6 comparisons between signals from river hydrometers RG1 and RG2 and the Ancona harbour tide gauge TG are proposed to evaluate

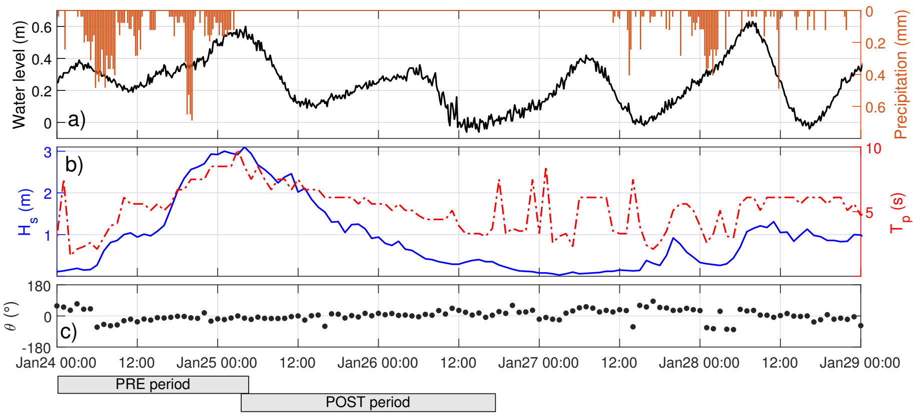

Figure 2: Wave climate in January 24–29. **a)** Water elevation as measured at the Ancona harbour (black line) and precipitation (orange bars). The datum is the mean sea level. **b)** Estimated significant wave height (blue line) and peak period (dashed red line) offshore of sensor QS2. **c)** Predominant direction of incoming waves with respect to the shore normal. The ranges of PRE and POST periods (Sections 3.1 and 3.2) are also labelled with the grey boxes.

the influence of tidal forcing over river discharge and water levels. The difference between signals at river hydrometers is made:

$$\eta_{\mathrm{diff}} = \eta_{\mathrm{RG1}} - \eta_{\mathrm{RG2}}, \tag{6}$$

and discrepancies between the tide gauge signal η_{TG} and η_{diff} are evaluated by means of a cumulative parameter defined as follows:

$$TGRG_{\mathrm{cum}} = \frac{1}{T_{\mathrm{rec}}} \sum (\eta_{\mathrm{TG}} - \eta_{\mathrm{diff}})\, \delta t, \tag{7}$$

where T_{rec} is the recording period over which the calculation is made and δt is the time discretization interval.

3. Results

3.1. Analysis of offshore sea state (sensor QS2)

The characterization of the sea state in front of the MR estuary is made by elaborating wave data measured seaward of and at sensor QS2, located approximately 650 m offshore of the river mouth. Figure 2 shows the offshore wave climate in front of the MR mouth as measured by an ADCP deployed seaward of QS2 between January 24 and January 29, 2014, when the wintertime section of the EsCoSed project took place [38]. The elevation datum for the water level in Figure 2 is the mean sea level. Precipitation data are collected from the database of the Civil Protection.[1]

The event occurring from January 24 to January 26, 2014 was a severe storm, characterized by offshore significant wave heights of up to 3 m during the first hours of January 25 (Figure 2a). The storm was sustained by strong northerly (Bora) winds, whose relatively short fetch in the Adriatic sea contributed to the generation of short and steep swells propagating almost perpendicularly to the shoreline (Figure 2c), also thanks to the relatively deep and engineered river mouth. Such swells were capable of penetrating the river mouth at least up to sensor QR2, where consistent wave oscillations were observed (Section 3.2). The storm was also accompanied by intense precipitation in terms of both rain rate and total daily rain [38].

The storm duration has been divided into two segments with a 1-hour overlapping. The PRE period, encompassing the storm growing up to its climax, spans from January 24, 00:00 to January 25, 05:00 (29 hours). The POST period, that includes the storm decay, runs from January 25, 04:00 to January 26, 18:00 (38 hours).

Figure 3 presents energy flux densities and evolution of band fluxes at offshore sensor QS2. The left panels show data from the PRE period, whereas right panels show data from the POST period.

In the PRE period, the offshore wave energy increased by nearly four orders of magnitude in the range 0–0.3 Hz throughout the investigated period (Figure 3a), the peak frequency being in the range of wind wave frequencies, 0.1–0.15 Hz (wave periods of 6.5–10 s) for both the initial calm state (January 24, 00:00–07:00; black to light grey spectra in Figure 3a) and the fully-developed storm condition (January 25, 00:00–05:00; orange and red spectra in Figure 3a).

[1] http://www.regione.marche.it/Regione-Utile/Protezione-Civile

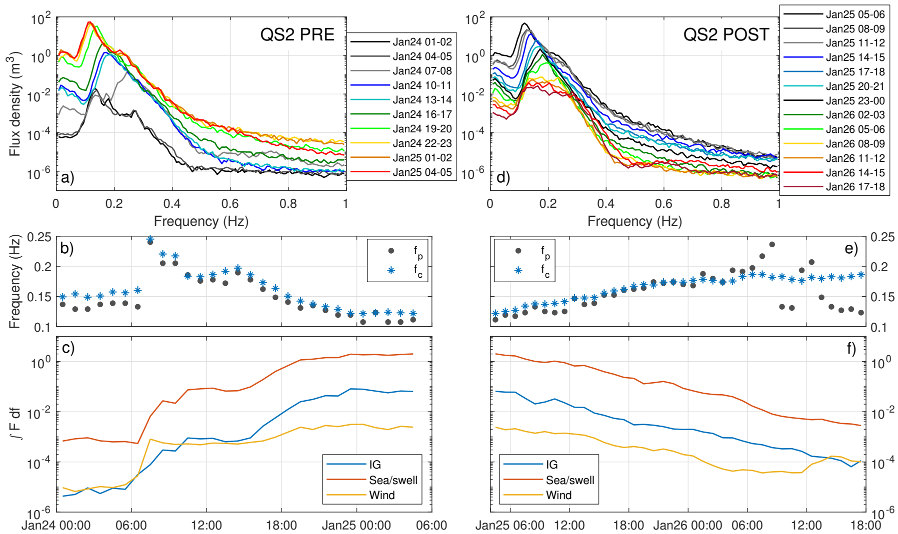

Figure 3: Evolution of energetic content at QS2 at selected hours during the PRE period (left panels) and the POST period (right panels) of the January 24–26 storm. **a) d)** Flux density spectra. **b) e)** Temporal evolution of the peak frequency f_p (grey dots) and the spectral centroidal frequency f_c (blue stars). **c) f)** Temporal evolution of integral fluxes for IG waves (blue line), SS waves (red line), and wind waves (yellow line).

At the very start of storm growth, on January 24, 07:00–08:00, the peak frequency showed an abrupt shift towards higher frequencies after January 24, 06:00 (see the light grey spectrum in Figure 3a and the peak in both f_p and centroidal frequency f_c in Figure 3b), due to short swell waves produced by sustained strong northerly winds that reached speeds up to 20 m/s (recorded by a weather station located within the harbor area) on relatively short fetches [38]. This is also confirmed by the coincident increase in integral flux for swell and wind wave frequencies (red and yellow lines in Figure 3c). As the storm increased its intensity, the bulk of storm energy transferred to lower frequencies and the peak frequency migrated back to the regular lower swell wave frequency range (0.1–0.15 Hz, see Figure 3b). The integral fluxes of IG and sea/swell waves seems to be proportional (compare blue and red lines in Figure 3c). In more detail, during the hours of storm climax, i.e. when the highest wave energy levels are attained, the IG wave energy E_{IG} increases with the sea-swell energy E_{ss} following a nonlinear trend, i.e. $E_{\mathrm{IG}} \propto E_{\mathrm{ss}}^{1.5}$ (Figure 4), in agreement with

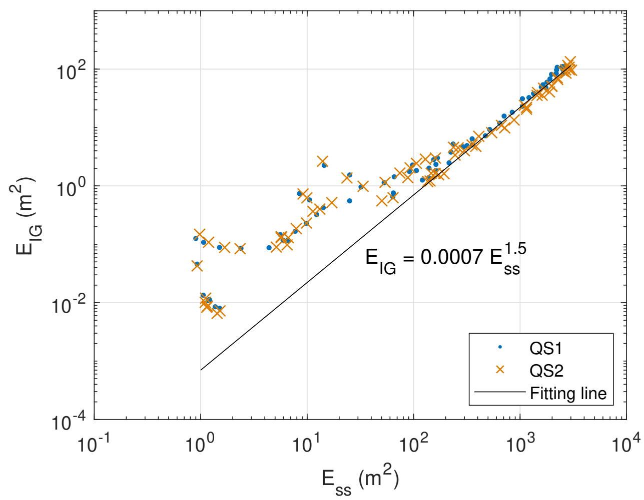

Figure 4: IG band energy E_{IG} versus sea/swell energy E_{ss} measured at QS1 (blue dots) and QS2 (orange crosses) across the investigated period. The black line represents a fitting line for the data with highest energy level.

previous literature findings [44].

Wind wave fluxes (yellow line in Figure 3c), on the other hand, quickly reached saturation after the steep increase in January 24, 06:00 and showed very little evolution afterwards, in spite of the storm growing steadily until January 25. Both IG and SS waves experienced more or less the same increase in absolute energy flux across storm growth up to the climax.

Offshore flux density spectra in the POST period are shown in Figure 3d. Also here, the peak frequency moved from the low swell frequency range (on January 25, 04:00–12:00; black to light grey spectra in Figure 3d) to higher frequencies (see Figure 3e), and the spectrum flattened until its typical peak shape is lost altogether and a clearly dominant frequency could not be singled out, although there still seems to be a dominance of low swell frequencies (on January 26, 11:00–18:00; yellow to red spectra in Figure 3d). Throughout storm decay, though, the frequency range pertaining to swell waves (0.05–0.3 Hz) lost up to four orders of energy content (Figure 3d). The same loss is retrieved in Figure 3f, where a steady decrease in energy flux is noticeable at all frequency bands and the link between IG and SS waves is again apparent.

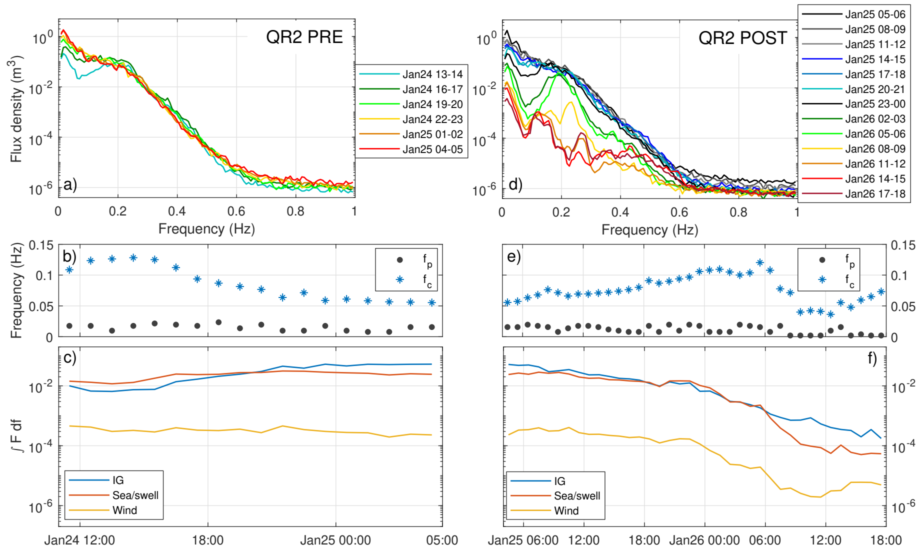

Figure 5: Evolution of energetic content at QR2 at selected hours during the PRE period (left panels) and the POST period (right panels) of the January 24–26 storm. **a) d)** Flux density spectra. **b) e)** Temporal evolution of the peak frequency f_p (grey dots) and the spectral centroidal frequency f_c (blue stars). **c) f)** Temporal evolution of integral fluxes for IG waves (blue line), SS waves (red line), and wind waves (yellow line).

3.2. Analysis of wave energy into the Misa River (sensor QR2)

The same analysis described in Section 3.1 has been also performed for sensor QR2, located within the final reach of the MR at about 400 m upstream of the mouth. As already evidenced in [38], the January 24–26 storm was energetic enough to drive waves up the channel in spite of the strong breaking outside the mouth, so a spectral analysis at this location is appropriate and gives a sense of how the wave energy content has evolved from the offshore to the river channel. The total measuring period is also here split into a PRE period and a POST period. Sensor QR2 was not in operation during the initial calm state, in January 25, 00:00–11:00.

Figure 5 presents selected flux density spectra and temporal evolution of band-specific fluxes at sensor QR2 during the PRE period (left panels) and the POST period (right panels). None of the spectral forms in the investigated period show peaks within the SS frequency range. Only the IG band (0–0.1 Hz) increased its energy flux by roughly one order of magnitude as the storm approached its climax; on the other hand, energy flux at wave frequencies greater than 0.15 Hz was largely unaltered (Figure 5a). The frequency peak was consistently inside the IG band (Figure 5b). Figure 5c also shows that the IG band had the largest increase in energy flux and eventually became the most energetic band after January 24, 18:00 (blue line in Figure 5c). Integral fluxes of swell and wind waves were largely unchanged, with the wind waves flux being particularly low. However, the centroidal frequency (blue stars in Figure 5b) falls in the sea-swell band at the earlier stages of the storm (this recalling the sea-swell dominance also in terms of integral fluxes, see Figure 5c) and towards the end of the storm (Figure 5e). This demonstrates the larger importance of the IG band during the core of the storm, while the sea-swell components gain more (relative) relevance into the river during the rise and fall stages of the storm, when both wave breaking and IG generation are reduced.

In the POST period the storm attenuation led to a general reduction of energy flux at all frequencies, although the energy loss was stronger for swell and low-frequency wind waves (0.15–0.4 Hz; see Figure 5d and yellow and red lines in Figure 5f). This is particularly evident in the spectra related to the end of the period, when a calm state characterized by a dominance of IG energy was achieved (orange to red spectra in Figure 5d). Also in the POST period the peak frequency f_p was located into the lower IG band at all times (0.01–0.03 Hz; see Figure 5e).

3.3. Wave setup

An estimate of wave-breaking-induced radiation stress in the area surrounding the MR estuary during the January 24–26 storm as been performed. Figure 6 gives space and time maps for the cross-shore radiation stress S_{xx} (left panel) and its cross-shore gradient $\mathrm{d}S_{xx}/\mathrm{d}x$ (right panel) along an ideal transect from the offshore into the river channel. The maps have been obtained by estimating and interpolating hourly values of radiation stress from both sea sensors (QS1 and QS2) and all river sensors (TGdown, QR1, QR2, QR3, and TGup).

The highest values of both radiation stress ($S_{xx} \approx 2500$ J/m^2) and its gra-

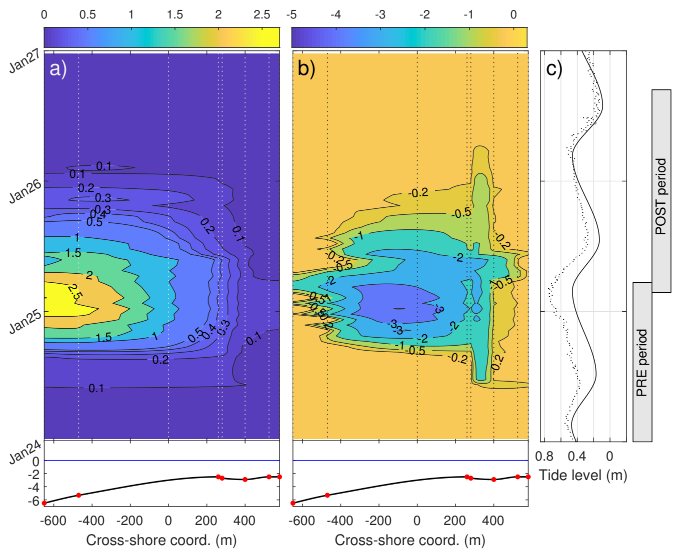

Figure 6: **a)** Cross-shore radiation stress S_{xx}, **b)** cross-shore gradient of S_{xx}, **c)** astronomical tide at Ancona (black line) and tidal level as measured at Ancona harbour (dotted line). Bottom panels represent the bottom profile. Dotted white lines in panels a) and b) and red dots in the bottom panels identify the position of sensors and the river mouth ($x = 0$ m). Positive x-coordinates are directed into the river. The ranges of PRE and POST periods are labelled with grey boxes.

dient ($\mathrm{d}S_{xx}/\mathrm{d}x \approx -5$ J/m^3) have been achieved at the hours of storm peak (January 25, 00:00–06:00). Strong alongshore gradients of S_{xx}, corresponding to wave-breaking-induced setups, occurred landward of sea sensor QS1 (470 m offshore of the mouth), where SS waves broke as an effect of reducing water depths. River current seems not to be strong enough to sufficiently enhance wave steepening and force waves to break. Specifically, during the Bora storm, the river current speed at the surface $U_{\text{river,surf}}$ never exceeds 1.0 m/s, and the maximum wave-induced horizontal velocity $U_{\text{wave,max}}$, estimated using linear wave theory, is comparable to such value. This leads to a ratio $U_{\text{river,surf}}/U_{\text{wave,max}} \leq 1.2$. On the other hand, based on simulations [3], much larger ratios are required ($U_{\text{river,surf}}/U_{\text{wave,max}} > 2.2$) to reach the condition of river-current-induced wave breaking. The absence of river current-induced wave breaking was also confirmed by visual observation.

The highest potential for wave-induced setup has been estimated right in front of the river mouth, up to 200 m offshore of it (second panel of Figure 6). Relevant setup gradients is also identified well into the river channel, al least up to sensor QR2, 400 m upriver from the mouth. Notably, a persistence of moderate radiation stress is observed in the region outside the mouth also in January 25, 12:00–18-00, simultaneously with low tide. Other than this, the patterns of radiation stress and its gradients seem not to be tide-modulated. An estimation of wave setup across a distance of $\mathcal{O}(100$ m), a typical length scale for local wave evolution, gives that maximum wave setups of around 0.05 m are expected to happen. Such values are small if compared to the local tide excursion (a few tens of centimeters) and the storm surge elevation, thus the relative importance of wave setup in raising mean water levels outside and into the estuary is expected to be low.

3.4. Interplay of sea and river currents

Figure 7 shows a comparison of depth-averaged current velocities and directions at river sensors QR1, QR2 and QR3 and sea sensor QS2 in the wintertime campaign (January 24–29), along with data from tides, precipitation and wave climate in the same period. See Figure 1 for the location of sensors.

At the most inland sensor QR1 (cyan diamonds in Figure 7c and d) seaward velocities reached up to 0.2 m/s until January 24, 10:00. River currents in this phase were strengthened by precipitation prior to the analyzed period. A slight upriver inversion of the current at QR1 is noticeable at the beginning of January 24, in association with a small flood tide and weak sea forcing.

A strong dominance of river flow was observed at QR2 (red squares in Figure 7c and d) with current velocities of more than 0.4 m/s throughout both storm build-up and decay. The peak velocity occurred around January 25, 06:00, about 11-12 hours after the strongest rainfall in January 24, 18:00–20:00. Despite a reduced influence of the wind stress on the river current (max $\sim 20-25\%$ of the total speed), the river outflow was strong to the point of generating a plume that propagated up to 1.3 km off the mouth [38], while halving the intensity and altering the prevalent direction of offshore currents measured at QS2 (pur-

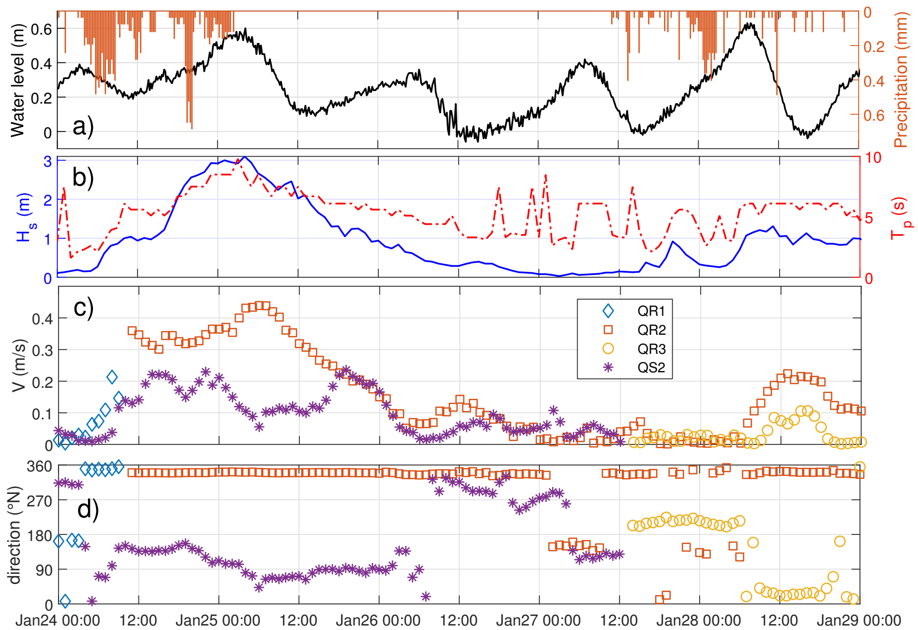

Figure 7: Interplay of river and sea forcings in the MR estuary. **a)** Tide at the Ancona harbour (black line) and precipitation (orange bars). The datum is the mean sea level.**b)** Offshore wave significant heights (blue line) and peak period (red dash-dotted line). **c)** Depth-averaged current velocities at river sensors QR1, QR2 and QR3 (cyan diamonds, red squares and yellow circles, respectively), and sea sensor QS2 (purple asterisks). **d)** Depth-averaged current directions at the same sensors.

ple stars in Figure 7c and d) during and immediately after storm peak. During storm decay sea and river currents were comparable, but the outflow still imparted a westward (seaward) orientation to the offshore current detected at QS2. The mean intensity and orientation of the river current at QR2 appeared not to be influenced by the alternating tide, although flow reversal was detected in January 27, 02:00–12:00, again in coincidence with flood tide and absent storm action. The river current, at least landward of sensor QR2, was strong enough to not be altered by tide- or wave-induced oscillations entering the channel, as already postulated in [38].

Only measurements from river sensors QR2 (red squares) and QR3 (yellow circles) are available in the period of the second, minor storm (January 27, 12:00 and afterwards). Prior to the development of the second storm the small currents detected at sensors QR2 and QR3 were oppositely oriented; mainly northerly oriented at QR2, and southerly oriented at QR3. This may suggest the presence of a convergence region between QR2 and QR3 in case of low river outflow, as evidenced also during the summertime campaign [38]. Afterwards, river currents at both sensors were directed seaward with maximum values in average flow velocity (0.2 m/s at QR2 and 0.1 m/s at QR3). No tide-induced oscillations in flow velocity or orientation were visible.

3.5. Propagation of low frequency waves in the lower reach of the Misa River

The temporal evolution for the total significant wave height H_{sig}, the IG contribution $H_{\mathrm{sig,IG}}$ and SS contribution $H_{\mathrm{sig,ss}}$ at sensors QS2 (offshore) and QR2 (into the river) for the January 24–26 storm is illustrated in Figure 8. While the most of the significant wave height at the offshore sensor QS2 was to be ascribed to the action of sea and swell waves, the contribution from the IG band $H_{\mathrm{sig,IG}}$ was up to 0.4 m at the peak of the storm and made for about 10–20% of the total height (top panel in Figure 8). Similar values of $H_{\mathrm{sig,IG}}$ about 0.4 m (corresponding to about 13% of the local water depth) have been observed at sensor QR2, 400 m from the mouth. This distance corresponds to about 10 times the local SS peak wavelength. In addition, the relative magnitude of

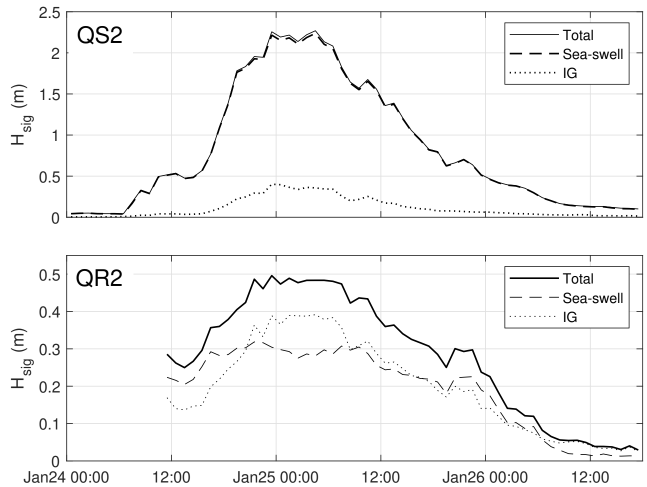

Figure 8: Band significant wave heights during the January 24–26 storm event at sensors QS2 (offshore; top panel), and QR2 (400 m into the river; bottom panel). The total height H_{sig}, SS contribution $H_{\mathrm{sig,ss}}$, and IG contribution $H_{\mathrm{sig,IG}}$ are represented with solid lines, dashed lines, and dotted lines respectively.

the IG contribution considerably increased in the river channel, to the point of reaching about 80% of the total wave height and overcoming the contribution of SS components in the hours of storm climax (bottom panel in Figure 8).

Presence of IG components up to the most inland river gauge is also apparent in Figure 9, in which maps of wave energy variation in time (the period of the first storm) and space (from the offshore to within the river mouth) are shown. For the maps in Figure 9 information from both sea sensors (QS1 and QS2) and all river sensors (TGdown, QR1, QR2, QR3, and TGup) have been elaborated and interpolated to obtain hourly estimates of wave energy from the offshore to into the river mouth. SS-band and IG-band wave energy (Figure 9b and c) are expressed as a percentage of the maximum total wave energy at the most offshore sensor, attained on January 25, 05:00. The SS-band-related energetic content experienced the largest decay as the river mouth is approached and entered, falling down to 10% of the total offshore magnitude (corresponding to $H_{\mathrm{sig,ss}} \approx 0.65$–$0.7$ m, about 21%–23% of the local water depth) at around 200 m past the mouth (about 10 times the offshore SS wavelength) and 2% at around

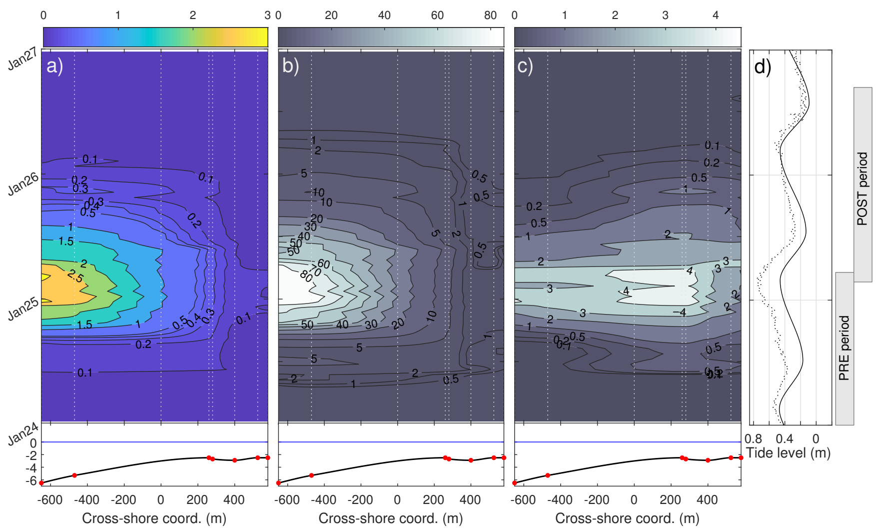

Figure 9: **a)** Total wave energy, **b)** percentage of SS wave energy (with respect to maximum offshore total wave energy), **c)** percentage of IG wave energy (with respect to maximum offshore total wave energy), **d)** astronomical tide at Ancona (black line) and tidal level as measured at Ancona harbour (dotted line). Bottom panels represent the bottom profile. Dotted white lines in panels a) to c) and red dots in the bottom panels identify the position of sensors and the river mouth ($x = 0$ m). Positive x-coordinates are directed into the river. The ranges of PRE and POST periods are labelled with grey boxes.

400 m ($H_{\mathrm{sig,ss}} \approx 0.25$ m, about 8% of the local water depth) even at the hours of strongest storm energy (Figure 9b). Conversely, the IG contribution underwent a modest enhancement in the river channel, where it held up to 4–5% of the maximum offshore wave energy ($H_{\mathrm{sig,IG}} \approx 0.45$–$0.5$ m, about 15–17% of local water depth) at storm peak, in a region within 300 m (15 times the offshore peak SS wavelength) upstream of the river inlet.

Figure 10a gives estimates of IG significant wave heights at river sensors TGdown and TGup. The evaluation of the IG waves attenuation rate R_{IG} (Equation (5)) between the two sensors is also performed. Values of R_{IG} are shown in Figure 10b. $H_{\mathrm{sig,IG}}$ of about 0.5 m (17% of local water depth) have been detected at TGdown in the hours of storm climax (January 25, 00:00–05:00; solid line in Figure 10a); in the same hours the IG wave height contribution at TGup, 300 m upriver of TGdown, was more than 0.3 m (10% of local water depth), resulting in R_{IG} of less than 40% as the wave field travels from TGdown

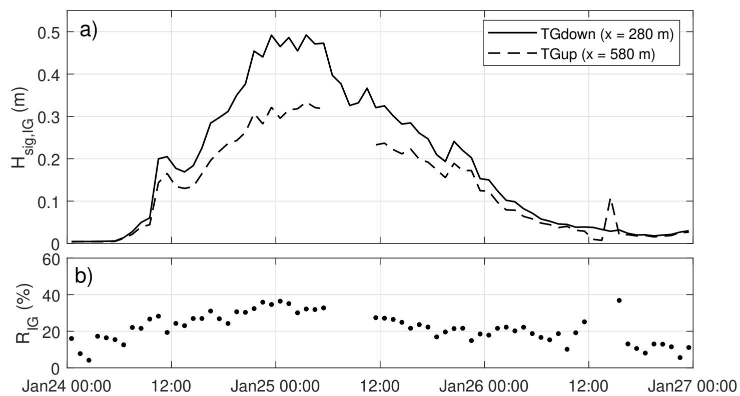

Figure 10: Decay of IG significant wave height throughout the river estuary. a) IG significant wave height $H_{\mathrm{sig,IG}}$ at sensors TGdown (280 m from river mouth; solid line) and TGup (580 m from river mouth; dashed line) during the January 24–26 storm event; b) reduction rates of $H_{\mathrm{sig,IG}}$.

to TGup (Figure 10b).

Figure 11 illustrates excerpts from signals at gauges TGdown (280 m upstream of the mouth) and TGup (580 m upstream of the mouth; Figure 1) on January 25, 00:00-00:20 are presented, along with the respective low-frequency components obtained through low-pass filtering. Patterns of low-frequency oscillations with zero-crossing periods ranging between 30 seconds and 3 minutes and amplitudes 0.1–0.4 m are clearly detectable beneath the SS wave train and can be retrieved at upward gauges at later times as they propagate (see the time shift of low-frequency components t_{lag} in Figure 11).

Table 1 provides estimates for IG components time lags between consecutive gauges at selected hours during the January 24–26 storm event, as well as for their propagation velocity. The test hours have been chosen as representative of the main stages of storm evolution. For each test hour, the first number is the estimate for the time shift t_{lag} of the IG wave component between two consecutive gauges, in seconds. Cross-correlation between IG signals at consecutive gauges always gave good results with correlation coefficients greater than 0.92 and p-values very close to 0 in all cases. The second number represents an estimate for the IG waves propagation velocity c_{IG} in m/s, as calculated with

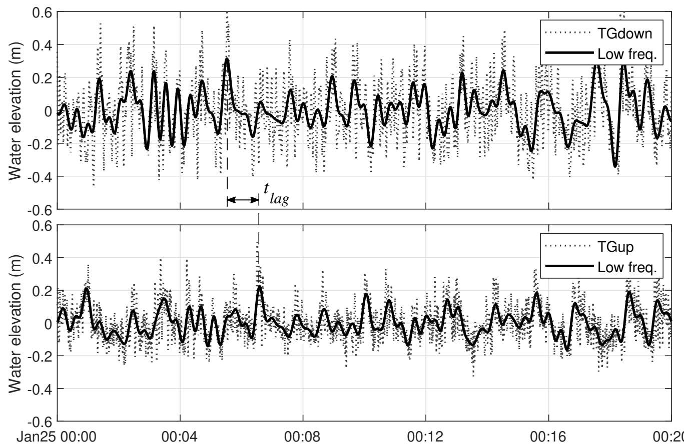

Figure 11: Time series of de-tided water elevation at sensors TGdown (280 m from river mouth; top panel) and TGup (580 m from river mouth; bottom panel) on January 25, 00:00–00:20. The dotted lines represent the de-tided signals; the low-frequency components obtained through low-pass filtering are shown with solid lines.

Equation (4). The estimates have been all computed between gauges TGdown and QR2 ($\Delta x \approx 120$ m; first row) and gauges QR2 and TGup ($\Delta x \approx 180$ m; second row), with the exception of the first test hour (January 24, 00-01; first column in Table 1). For this hour, only a correlation between gauges TGdown and TGup ($\Delta x \approx 300$ m) could have been established since QR2 was not operative at that time.

Table 2 shows estimates for phase speeds at sensor QR2 during the same

Table 1: Estimates of time lags and velocity propagation of low-frequency wave components into the Misa River estuary during the January 24–26 storm event. The tags under the hours indicate the storm stage.

Gauge	**Hour**									
	Jan 24, 00-01 [*calm*]		Jan 24, 12-13 [*storm rise*]		Jan 25, 00-01 [*climax*]		Jan 25, 18-19 [*storm fall*]		Jan 26, 08-09 [*calm*]	
	t_{lag} [s]	c_{IG} [m/s]	t_{lag} [s]	c_{IG} [m/s]	t_{lag} [s]	c_{IG} [m/s]	t_{lag} [s]	c_{IG} [m/s]	t_{lag} [s]	c_{IG} [m/s]
TGdown										
			24.5	4.9	22	5.5	23.5	5.1	23.5	5.1
QR2	67.5	4.4								
			50	3.6	45.5	4.0	46.5	3.9	46.5	3.9
TGup										

storm. Reported are also the depth-averaged current velocities V at QR2 on the same hours (also shown in Figure 7). Assuming a mean undisturbed water depth $h = 3.1$ m at QR2, the linear theory shallow water speed $c = \sqrt{gh}$ is equal to 5.5 m/s. The observed perturbation to the mean (undisturbed) water depth, $\langle\eta\rangle$ (made of proper tide elevation and contributions from storm-related wave setup and storm surge) ranged from -0.2 to $+0.25$ m/s. This leads to a modified phase speed $c^* = \sqrt{g\,(h + \langle\eta\rangle)}$ between a minimum of 5.33 m/s in January 24, 12:00–13:00, when storm rising was paired with low tide (Figure 2), and a maximum of 5.73 m/s in January 25, 00:00–01:00, when the storm climax was paired with high tide (Figure 2) and the propagation velocity of the low-frequency signal reached its maximum value both for the TGdown–QR2 (5.5 m/s) and the QR2–TGup (4.0 m/s) intervals (Table 1).

When the storm was rising and the effect of storm-related setup and surge should thus increase (January 24, 12:00–13:00), low tide dominated by giving a total negative mean water elevation ($\langle\eta\rangle$ = -0.2 m; Table 2). Also during storm climax in high tide (January 25, 00:00–01:00), when all agents in water level variation (tide, surge, and setup) are at their maximum potential, surge and setup are accountable for only a minor part of the mean water level elevation $\langle\eta\rangle$ achieved at that hour. A tidal positive excursion is expected of the same magnitude of the negative excursion, 0.2 m. Since the total observed excursion is $\langle\eta\rangle = +0.25$ m, tide alone is accountable for around 80% of the total excursion, with the total effect of setup and surge being roughly 20%.

A fair approximation of estimated c_{IG} between TGdown and QR2 can be done by subtracting mean river flow velocities V from the theoretical speeds c^*. This gives slightly underestimated values in storm climax with high tide ($c^* - V = 5.73 - 0.37 = 5.36$ m/s, comparable with $c_{\mathrm{IG}} = 5.5$ m/s), and slightly overestimated values during both storm rise ($c^* - V = 4.98$ m/s, comparable with $c_{\mathrm{IG}} = 4.9$ m/s) and storm fall ($c^* - V = 5.11$–5.19 m/s, comparable with $c_{\mathrm{IG}} = 5.1$ m/s).

Tables 3 and 4 collect the same estimates evaluated for selected hours during the second major storm event, occurred on January 28–29. The second storm

Table 2: Evaluation of modified phase speeds at sensor QR2 (h = 3.1 m) during the January 24–26 storm event. The tags under each hour indicate the storm stage and the tide stage. High tide and low tide are marked in bold. The elevation of mean water level $\langle\eta\rangle$ is evaluated as excursion from the undisturbed water depth h. $c^* = \sqrt{g\,(h + \langle\eta\rangle)}$ is the modified phase speed.

	Hour							
	January 24		January 25				January 26	
	12–13	19–20	00–01	08–09	12–13	18–19	00–01	08–09
	[*rise*]	[*rise*]	[*climax*]	[*fall*]	[*fall*]	[*fall*]	[*fall*]	[*calm*]
	[**low**]	[*flood*]	[**high**]	[*ebb*]	[**low**]	[*flood*]	[*flood*]	[**high**]
$\langle\eta\rangle$ [m]	-0.2	0	+0.25	0	-0.1	-0.1	-0.05	0
c_{NL} [m/s]	5.33	5.51	5.73	5.51	5.42	5.42	5.47	5.51
V [m/s]	0.35	0.32	0.37	0.4	0.31	0.23	0.15	0.07

was less energetic than the previous one due to weaker winds characterized by an almost constant direction for a shorter period [38]. This led to water surface levels oscillating between -0.25 m and 0.25 m, while a complete tide cycle occurred. Specifically, almost constant wave heights ($H_s \sim 0.5$ m) were recorded between the two high tides, with no apparent influence from the tide phase, as shown in Figure 12. On the other hand, the tidal level played a major role over the propagation velocity of low frequency components in spite of the microtidal nature of the estuary, mainly by increasing water heights into the river and thus letting waves propagate with a larger celerity (see Table 3). High tide on January 28, 07:00–08:00 and January 29, 08:00–09:00 promoted a quicker propagation of low frequency waves thanks to higher water columns within the channel. The effect of high tide was felt up to TGup, the most landward tide gauge inside the river, giving slightly higher c_{IG} also between QR2 and TGup (see the second and sixth columns in Table 3). The lowest c_{IG}, conversely, were attained on January 28, 15:00–16:00 (fourth column in Table 3), when low tide led to a strongly negative $\langle\eta\rangle$ (-0.55 m; Table 4) in spite of storm climax. The major influence of tide is also highlighted by the fact that positive mean water elevation $\langle\eta\rangle$ is achieved even for a falling storm (January 29, 08:00–09:00). Also for the second storm, $c^* - V$ gives slightly overestimated values of c_{IG} for both storm rise in high tide ($c^* - V = 5.58$ m/s if compared to 5.4 m/s) and storm climax in low tide ($c^* - V = 4.79$ m/s if compared to 4.6 m/s).

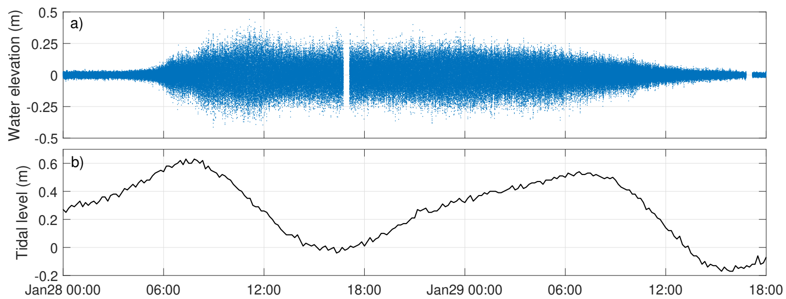

Figure 12: **a)** De-tided and de-trended water elevation time series for the January 28–29 storm event at TGdown. **b)** Storm tide level as measured in Ancona harbour during the same period.

Table 3: Estimates of time lags and velocity propagation of low-frequency wave components into the Misa River estuary during the January 28–29 storm event. The tags under the hours indicate the storm stage.

Gauge	**Hour** Jan 28, 01-02		Jan 28, 07-08 [*high tide*]		Jan 28, 11-12		Jan 28, 15-16 [*low tide*]		Jan 29, 01-02		Jan 29, 08-09 [*high tide*]	
	t_{lag} [s]	c_{IG} [m/s]	t_{lag} [s]	c_{IG} [m/s]	t_{lag} [s]	c_{IG} [m/s]	t_{lag} [s]	c_{IG} [m/s]	t_{lag} [s]	c_{IG} [m/s]	t_{lag} [s]	c_{IG} [m/s]
TGdown												
	22	5.4	22	5.4	23.5	5.1	26	4.6	24	5.0	23	5.2
QR2												
	46	3.9	43.5	4.1	47.5	3.8	51.5	3.5	47	3.8	46	3.9
TGup												

Table 4: Evaluation of modified phase speeds at sensor QR2 (h = 3.1 m) during the January 28–29 storm event. The tags under each hour indicate the storm stage and the tide stage. High tide and low tide are marked in bold. The elevation of mean water level $\langle\eta\rangle$ is evaluated as excursion from the undisturbed water depth h. $c^* = \sqrt{g\,(h + \langle\eta\rangle)}$ is the modified phase speed.

	Hour January 28				January 29	
	01–02 [*calm*] [*flood*]	07–08 [*rise*] [**high**]	11–12 [*climax*] [*ebb*]	15–16 [*climax*] [**low**]	01–02 [*climax*] [*flood*]	08–09 [*fall*] [**high**]
$\langle\eta\rangle$ [m]	-0.15	+0.15	-0.2	-0.55	-0.1	+0.2
c_{NL} [m/s]	5.38	5.65	5.33	5	5.42	5.69
V [m/s]	0	0.07	0.19	0.21	–	–

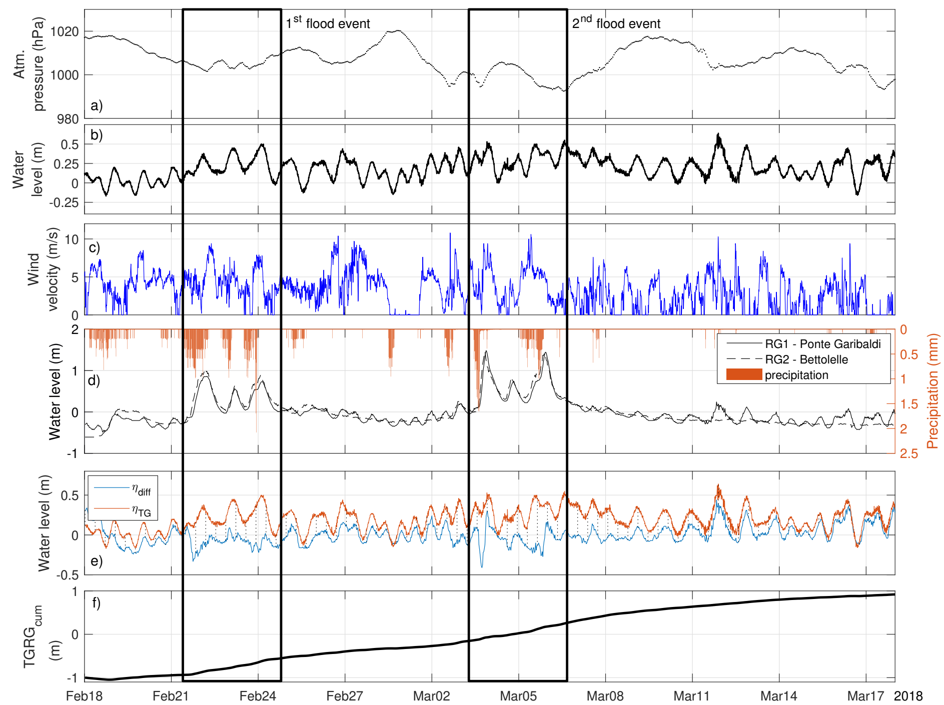

Figure 13: Measurements collected by the tide gauge in Ancona harbour in February-March 2018 and comparison with river gauge measurements. **a)** Atmospheric pressure, **b)** water level (the ordnance datum is the mean sea level), and **c)** wind velocity at the Ancona harbour. **d)** Comparison between water level observations at river gauges RG1 (1.5 km from estuary mouth; solid black line) and RG2 (10 km from estuary mouth; dashed black line), and precipitation levels (orange bars). **e)** Difference between hydrometer measurements (η_{diff}, blue line) compared with storm tide (η_{TG}, orange line). **f)** Cumulative difference between η_{TG} and η_{diff}. The two major flood events are evidenced in black boxes.

3.6. Interaction between tide and river forcings in the Misa River

In view of the ascertained role of tidal action over wave propagation dynamics in the MR estuary, the sea surface oscillations recorded by the tide gauge in the harbour of Ancona (TG hereafter) is here compared to data from the hydrometers at “Ponte Garibaldi” and “Bettolelle” (respectively RG1 and RG2 in Figure 1) to better understand the penetration of tidal forcing into the MR estuary. Figure 13a–c illustrate data of atmospheric pressure, water level and wind speed recorded at TG in February–March 2018, while Figure 13d–f show measurements at TG, RG1 and RG2, as well as precipitation data.

The February–March 2018 time period has been chosen because the recorded conditions are comparable to those observed during the Bora storm occurred on 24–26 January 2014 (see [38] for comparison), when measurements at RG1 and RG2 were not available. Specific high-flow conditions have been identified in two distinct time ranges, i.e. February 21–24 and March 3–6 (see black boxes in Figure 13). Although they seem to show periods of about 24 hours, the three contiguous peaks in water level at RG1 and RG2 during these high-flow events are due to both the time interval between contiguous precipitations and the hydrologic routing of precipitation through the MR watershed t_c.

Five rainfall gauges have also been selected[2] to evaluate the mean precipitation on the MR watershed (orange bars in Figure 13d). Three significant precipitation events (1–2.5 mm) occurred in February, just before the peaks in the first flood event, and two significant events (1–2 mm) occurred in March, just before two flood peaks in the second flood event.

Oscillations periods of 12 to 24 hours are observed at the downstream gauge RG1 (see also [42]) in phase with tidal cycles at TG. This shows that tide reached relatively large distances from the river mouth, especially during low- to moderate-flow conditions, although the MR environment is classified as microtidal. To better analyze this aspect, the TG recordings (η_{TG}) have been compared to the difference between RG1 and RG2 measurements (η_{diff}; see Equation (6)), with the aim to remove the river forcing effects, similar at RG1 and RG2, and highlight the tide influence. Figure 13e shows that the two time series are in phase during low-flow conditions (outside the black boxes) and suggests that the tide only affected RG1, with negligible effects on RG2. On the other hand, η_{diff} and η_{TG} are not in phase during flood events (inside the black boxes); this suggests that, in high-flow conditions, the river forcing largely prevailed over tide action and prevented the tide from reaching the downstream station.

[2] Regional database of the "Centro Funzionale Multirischi per la Meteorologia, l'Idrologia e la Sismologia", Marche Region

4. Discussion

4.1. Evolution of wave components

The January 24–26 storm featured an intense sea state with a sustained energy injection at high frequencies and a homogeneous redistribution of energy among all frequencies as the storm reached its climax (left panels of Figure 3). A link between swell waves and low-frequency waves is apparent across the whole storm. This can be explained by IG wave frequencies receiving energy from shorter wave frequencies, typically as a byproduct of several mechanisms like nonlinear interactions, shoaling and bore merging in the surf zone [5, 12, 14]. Although nonlinear interactions between sea/swell components may occur in the shoaling zone and generate IG waves, the bound wave mechanism [5] seems to be the dominant IG generation process in the coastal zone of the MR estuary. Such mechanism is typical of mild slope regimes characterized by a normalized slope parameter $\beta_b < 0.3$ [45]:

$$\beta_b = \frac{h_x}{\omega}\sqrt{\frac{g}{h}}, \tag{8}$$

where h_x is the bed slope, ω the wave angular frequency, and h a characteristic depth value. For the studied area, $h_x \sim 0.005$, while the dominant offshore wave frequency during storm climax is $f = 0.1$ Hz (Figure 3b), which provides $\omega = 0.63$ rad/s. Since off the mouth the typical depth is $h = (3\text{–}6)$ m, β_b is around 0.010–0.014, suggesting a dominance of the bound wave mechanism.

Storm decay, conversely, showed an homogeneous reduction of energy flux at all frequencies, with the SS frequency range still being energetically dominant (right panels of Figure 3).

As waves moved into the channel, IG motions gained a more relevant role over swell and wind waves. As the storm intensified offshore, the IG band experienced the largest increment in flux energy density into the river while SS energy was unaltered (left panels of Figure 5). This was favoured by intense wave breaking and energy dissipation affecting mainly SS components outside the river inlet (Figure 6).

The contribution of IG waves to wave height in the river closely followed the offshore significant wave height [28, 46] and reached values of 0.5 m, 0.4 m and 0.3 m respectively 280 m, 400 m and 600 m from the river mouth (Figures 8 and 10). This corresponds to a decay from about 25% of the local depth at QR3, to about 10% of the local depth at TGup. The contribution of sea and swell, on the other hand, came to saturation (bottom panel of Figure 8) and is reflected by a sharp drop in wave energy (Figure 9).

Moreover, due to a river discharge evaluated as $Q = (45 - 50)$ m^3/s during the storm peak and to the plume extending up to 1.3 km off the mouth [38], the increased average velocity of the river flow evidenced after intense rainfall in January 24 (up to 0.45 m/s at 400 m from the mouth) was strong to the point of damping and deviating storm-driven sea currents as much as 650 m offshore of the river mouth (Figure 7), but not enough to block low frequency waves. This is in agreement with observations at the Albufeira Lagoon inlet [30], where gravity waves are damped as long as the ebb-tidal delta is crossed, and IG waves propagate beyond the inlet provided the opposing current (given by ebb tidal flows) is not strong enough.

Low-frequency components manage to hold moderate, tide-modulated propagation speeds that are always directed upriver (in the range 3.6–5.5 m/s; Tables 1 and 3). Tide is indeed dominant over storm surge and wave setup in controlling the upriver propagation velocity of IG components against the river current.

Overall, we can say that the MR estuary and nearshore zone acted as a low-pass filter capable of removing higher-frequency waves (dissipation outside the mouth) while retaining low-frequency energy. A similar behaviour has been so far observed and documented only for oceanic inlets. IG waves propagating upstream as bores have been identified at the Pescadero inlet [28]. Similarly, fluctuations in the IG range, responsible for up to 50% of flow velocity oscillations, have been observed in the Albufeira Lagoon [2, 29], and IG velocity amplitudes of 0.1 m/s are detected in the Ría de Santiuste estuary [37]. These inlets are subjected to higher tide excursions, periodic cut-off from the open sea and much more severe wave regimes than the MR estuary (tidal excursions between 1.4 m and 3.6 m and significant wave height between 1.9 m and 4 m). No studies of IG energy propagation have been performed for inlets with low tide excursion, to the best of authors' knowledge. Therefore, our work marks the first observations of such "filtering effect" in a microtidal setting and comparatively milder wave climates common in enclosed basins like the Adriatic Sea.

We expect that the highly engineered final reach of the MR, the effects of which are not investigated in this work, might play a role on the observed phenomena. Uncles et al [37] suggested that the dominant frequencies of IG waves penetrating into the Ría de Santiuste are close to resonance periodicities typical of that estuary, and their effects are thus possibly amplified by resonance. The concrete jetties that bound the flow of the MR in its final stretch may have a similar effect and furnish an explanation to the focussing and amplification of IG waves energy observed inside the channel, up to 300 m landward of the mouth (Figure 9c). Our data sets, however, did not allow us further analyses on this regard.

4.2. Influence of tide in the estuary

Several studies [1, 28, 30, 47, 48] have ascertained that tide and related processes are crucial factors in determining how much of the incident wave energy is able to cross an inlet mouth or estuary, by inducing depth-limited wave breaking over shoals and bars [48] and enhancing/reducing residual wave heights in backbarrier lagoons and estuaries when associated to ebb/flood currents [1, 2, 30, 47]. These observations, though, are often obtained for coastal environments with significant tidal excursions.

Our study proposes novel findings that tide exerts some effect also in microtidal estuaries. In particular, similarly to what observed in macrotidal environments (see Figures 7 and 8 in [30] as an example), it is shown that the tide has a fundamental role in controlling the upriver propagation of IG waves. Further, IG waves propagation velocities are enhanced during flood tide and high tide (Table 3), mainly due to an increase of water levels into the estuary. The majority of the water levels increment has to be ascribed to tide also in the phases of greatest storm intensity, when the combined effect of storm-induced setup and surge account for no more than 20% of the total mean water elevation. Moreover, albeit the tidal range at the MR estuary is low (less than 0.6 m between high tide and low tide in the investigated period), tidal oscillations are visible at all river sensors up to 1.5 km from the mouth (Figure 13). Tidal currents in the MR estuary, conversely, are low and rarely affect the mean velocity and orientation of the river current (Figure 7). The MR current is directed upriver only when flood/high tide occurs in coincidence with low-flow conditions in both river and sea. Other than this, river forcing is generally dominant over tide in wintertime conditions, and the effect of tide is obliterated during river floods, as observed in [38].

Wave setup, forced by wave breaking and energy dissipation in front of the estuary mouth, was relatively small and not critically modulated by the tide. Nonetheless, the tide is shown to promote some persistence of wave-induced setup in the region immediately off the estuary, where moderate gradients of radiation stress appear to be maintained by low tide [2] during storm decay (Figure 6).

5. Conclusions

The present study inspected the hydrodynamic behaviour of the microtidal, wave-dominated estuary of the Misa River (Italy). Microtidal inlets with wave dominance are common along the Adriatic Sea. Analysis of field measurements during a storm event in January 2014 and signals from hydrometers in February–March 2018 allowed us to observe evolutionary trends for waves of different frequencies (SS waves, IG waves, and tide) both offshore and into the river mouth.

For the first time, the mechanism of “low-pass filtering” of wave energy exerted by several tide-dominated inlets around the world [2, 28, 30] has been assessed also for a microtidal environment. In tide-dominated inlets, wave propagation, enhancement and dissipation are often altered by strong ebb/flood currents [2, 30]. Inlets and back-barrier lagoons may get "cut off" from offshore wave action during low tides [28]. In coasts characterized by relevant sediment transport dynamics, inlets may also be filled by the concurrent action of tide and waves [29]. All the aforementioned processes may modify the penetration of wave energy in a significant way. This study demonstrates that also in a microtidal estuary, with near-zero tidal currents and always in connection with the sea, a natural filtering of wave frequencies occurs.

High-frequency storm waves from wind and swell strongly dissipate and decay outside of the MR mouth in the most seaward portion of the river, their energy contribution being negligible after 400 m from the inlet. Low frequency (IG) waves, on the other hand, slightly increased their relative energy and eventually overpowered high-frequency oscillations in the channel. Short wave dissipation is promoted by shoaling and breaking processes in shallow depths, as well as by strong opposing river currents after heavy rainfall. The enhanced river flow, though, is not able to dampen low frequency waves as much as strong ebb currents do in tidal inlets [2, 30].

In spite of the microtidal nature of the MR estuary, tidal action is felt across a large distance. In the final reach of the river, high tide promotes a faster IG waves upriver propagation by means of increased water depths. Tidal oscillations are also detected across all river sensors except the most landward one, particularly during low- to moderate-flow conditions. Due to the modest tidal excursions, however, tidally-generated currents are not able to alter river flows significantly, if not during extremely low river flow regimes.

A more detailed analysis would surely benefit from other comprehensive, simultaneous measurements of waves, tides, and river discharge. Information from a video-monitoring station recently installed near the estuary, moreover, would complement the study with a reconstruction of morphodynamic features in the nearshore. Finally, although we believe it may have a determinant role, the effects of river engineering on the processes studied in this work and the potential for phenomena of wave resonance have not been investigated. All of the abovementioned aspects will have to be analyzed in future research.

6. Acknowledgments

The financial support from the Office of Naval Research Global (UK) MORSE Project (Research Grant N62909-17-1-2148) is acknowledged. Joe Calantoni was supported under base funding to the U.S. Naval Research Laboratory from the Office of Naval Research.

References

[1] M. Olabarrieta, J. C. Warner, N. Kumar, Wave-current interaction in Willapa Bay, Journal of Geophysical Research 116 (C12). doi:10.1029/2011jc007387.
URL https://doi.org/10.1029/2011jc007387

[2] G. Dodet, X. Bertin, N. Bruneau, A. B. Fortunato, A. Nahon, A. Roland, Wave-current interactions in a wave-dominated tidal inlet, Journal of Geophysical Research: Oceans 118 (3) (2013) 1587–1605. doi:10.1002/jgrc.20146.
URL https://doi.org/10.1002/jgrc.20146

[3] M. Olabarrieta, W. R. Geyer, N. Kumar, The role of morphology and wave-current interaction at tidal inlets: An idealized modeling analysis, Journal of Geophysical Research: Oceans 119 (12) (2014) 8818–8837. doi:10.1002/2014jc010191.
URL https://doi.org/10.1002/2014jc010191

[4] L. Cui, H. Huang, C. Li, D. Justic, Lateral circulation in a partially stratified tidal inlet, Journal of Marine Science and Engineering 6 (4) (2018) 159. doi:10.3390/jmse6040159.

[5] X. Bertin, A. de Bakker, A. van Dongeren, G. Coco, G. André, F. Ardhuin, P. Bonneton, F. Bouchette, B. Castelle, W. C. Crawford, M. Davidson, M. Deen, G. Dodet, T. Guérin, K. Inch, F. Leckler, R. McCall, H. Muller, M. Olabarrieta, D. Roelvink, G. Ruessink, D. Sous, É. Stutzmann, M. Tissier, Infragravity waves: From driving mechanisms to impacts, Earth-Science Reviews 177 (2018) 774–799. doi:10.1016/j.earscirev.2018.01.002.
URL https://doi.org/10.1016/j.earscirev.2018.01.002

[6] R. Davidson-Arnott, An Introduction to Coastal Processes and Geomorphology, Cambridge University Press, 2009. doi:10.1017/cbo9780511841507.

[7] W. H. Munk, Origin and generation of waves, in: Proceedings of the First Conference on Coastal Engineering. Long Beach, California, 1950.

[8] M. J. Tucker, Surf beats: sea waves of 1 to 5 min. period, Proceedings of the Royal Society of London. Series A. Mathematical and Physical Sciences 202 (1071) (1950) 565–573. doi:10.1098/rspa.1950.0120.

[9] M. Longuet-Higgins, R. Stewart, Radiation stresses in water waves; a physical discussion, with applications, Deep Sea Research and Oceanographic Abstracts 11 (4) (1964) 529–562. doi:10.1016/0011-7471(64)90001-4.

[10] G. Symonds, D. A. Huntley, A. J. Bowen, Two-dimensional surf beat: Long wave generation by a time-varying breakpoint, Journal of Geophysical Research 87 (C1) (1982) 492. doi:10.1029/jc087ic01p00492.

[11] T. H. C. Herbers, S. Elgar, R. T. Guza, Generation and propagation of infragravity waves, Journal of Geophysical Research 100 (C12) (1995) 24863–24872. doi:10.1029/95jc02680.
URL https://doi.org/10.1029/95JC02680

[12] B. Ruessink, Bound and free infragravity waves in the nearshore zone under

breaking and nonbreaking conditions, Journal of Geophysical Research: Oceans 103 (C6) (1998) 12795–12805.

[13] B. Ruessink, The temporal and spatial variability of infragravity energy in a barred nearshore zone, Continental Shelf Research 18 (6) (1998) 585–605. doi:10.1016/s0278-4343(97)00055-1.

[14] A. Sheremet, R. T. Guza, S. Elgar, T. Herbers, Observations of nearshore infragravity waves: Seaward and shoreward propagating components, Journal of Geophysical Research 107 (C8) (2002) 10–1 – 10–10. doi:10.1029/2001jc000970.

[15] A. Reniers, J. MacMahan, E. Thornton, T. Stanton, Modelling infragravity motions on a rip-channel beach, Coastal Engineering 53 (2-3) (2006) 209–222. doi:10.1016/j.coastaleng.2005.10.010.

[16] A. Sheremet, J. Kaihatu, S.-F. Su, E. Smith, J. Smith, Modeling of nonlinear wave propagation over fringing reefs, Coastal Engineering 58 (12) (2011) 1125–1137. doi:10.1016/j.coastaleng.2011.06.007.

[17] K. Inch, M. Davidson, G. Masselink, P. Russell, Observations of nearshore infragravity wave dynamics under high energy swell and wind-wave conditions, Continental Shelf Research 138 (2017) 19–31. doi:10.1016/j.csr.2017.02.010.

[18] O. Billson, P. Russell, M. Davidson, Storm waves at the shoreline: When and where are infragravity waves important?, Journal of Marine Science and Engineering 7 (5) (2019) 139. doi:10.3390/jmse7050139.

[19] M. Brocchini, Wave-forced dynamics in the nearshore river mouths, and swash zones, Earth Surface Processes and Landforms (2019). doi:10.1002/esp.4699.

[20] R. T. Guza, E. B. Thornton, Swash oscillations on a natural beach, Journal of Geophysical Research 87 (C1) (1982) 483. doi:10.1029/jc087ic01p00483.

[21] B. Raubenheimer, R. Guza, Observations and predictions of run-up, Journal of Geophysical Research: Oceans 101 (C11) (1996) 25575–25587.

[22] P. Ruggiero, Wave run-up on a high-energy dissipative beach, Journal of Geophysical Research 109 (C6). doi:10.1029/2003jc002160.

[23] R. A. Beach, R. W. Sternberg, Suspended sediment transport in the surf zone: Response to cross-shore infragravity motion, Marine Geology 80 (1-2) (1988) 61–79. doi:10.1016/0025-3227(88)90072-2.

[24] R. A. Beach, R. W. Sternberg, Infragravity driven suspended sediment transport in the swash, inner and outer-surf zone, in: Coastal Sediments, ASCE, 1991, pp. 114–128.

[25] T. Aagaard, B. Greenwood, Infragravity wave contribution to surf zone sediment transport — the role of advection, Marine Geology 251 (1-2) (2008) 1–14. doi:10.1016/j.margeo.2008.01.017.

[26] T. Baldock, P. Manoonvoravong, K. S. Pham, Sediment transport and beach morphodynamics induced by free long waves, bound long waves and wave groups, Coastal Engineering 57 (10) (2010) 898–916. doi:10.1016/j.coastaleng.2010.05.006.

[27] A. T. M. de Bakker, J. A. Brinkkemper, F. van der Steen, M. F. S. Tissier, B. G. Ruessink, Cross-shore sand transport by infragravity waves as a function of beach steepness, Journal of Geophysical Research: Earth Surface 121 (10) (2016) 1786–1799. doi:10.1002/2016jf003878.

[28] M. E. Williams, M. T. Stacey, Tidally discontinuous ocean forcing in bar-built estuaries: The interaction of tides, infragravity motions, and frictional control, Journal of Geophysical Research: Oceans 121 (1) (2016) 571–585. doi:10.1002/2015jc011166.
URL https://doi.org/10.1002/2015JC011166

[29] X. Bertin, D. Mendes, K. Martins, A. B. Fortunato, L. Lavaud, The closure of a shallow tidal inlet promoted by infragravity waves, Geophysical Research Letters 46 (12) (2019) 6804–6810. doi:10.1029/2019gl083527.

[30] X. Bertin, M. Olabarrieta, Relevance of infragravity waves in a wave-dominated inlet, Journal of Geophysical Research: Oceans 121 (8) (2016) 5418–5435. doi:10.1002/2015jc011444.
URL http://dx.doi.org/10.1002/2015JC011444

[31] A. V. Dongeren, R. Lowe, A. Pomeroy, D. M. Trang, D. Roelvink, G. Symonds, R. Ranasinghe, Numerical modeling of low-frequency wave dynamics over a fringing coral reef, Coastal Engineering 73 (2013) 178–190. doi:10.1016/j.coastaleng.2012.11.004.

[32] D. Roelvink, A. Reniers, A. van Dongeren, J. van Thiel de Vries, R. McCall, J. Lescinski, Modelling storm impacts on beaches, dunes and barrier islands, Coastal Engineering 56 (11-12) (2009) 1133–1152. doi:10.1016/j.coastaleng.2009.08.006.

[33] M. Okihiro, R. T. Guza, R. J. Seymour, Excitation of seiche observed in a small harbor, Journal of Geophysical Research 98 (C10) (1993) 18201. doi:10.1029/93jc01760.

[34] M. Okihiro, R. T. Guza, Observations of seiche forcing and amplification in three small harbors, Journal of Waterway, Port, Coastal, and Ocean Engineering 122 (5) (1996) 232–238. doi:10.1061/(asce)0733-950x(1996)122:5(232).

[35] J. L. Luick, J. B. Hinwood, Water levels in a dual-basin harbour in response to infragravity and edge waves, Progress in Oceanography 77 (4) (2008) 367–375. doi:10.1016/j.pocean.2006.04.002.

[36] D. T. Thotagamuwage, C. B. Pattiaratchi, Observations of infragravity period oscillations in a small marina, Ocean Engineering 88 (2014) 435–

445. doi:10.1016/j.oceaneng.2014.07.003.
URL https://doi.org/10.1016/j.oceaneng.2014.07.003

[37] R. Uncles, J. Stephens, C. Harris, Infragravity currents in a small ría: Estuary-amplified coastal edge waves?, Estuarine, Coastal and Shelf Science 150 (2014) 242–251. doi:10.1016/j.ecss.2014.04.019.
URL https://doi.org/10.1016/j.ecss.2014.04.019

[38] M. Brocchini, J. Calantoni, M. Postacchini, A. Sheremet, T. Staples, J. Smith, A. H. Reed, E. F. Braithwaite, C. Lorenzoni, A. Russo, S. Corvaro, A. Mancinelli, L. Soldini, Comparison between the wintertime and summertime dynamics of the Misa River estuary, Marine Geology 385 (2017) 27–40. doi:10.1016/j.margeo.2016.12.005.
URL https://doi.org/10.1016/j.margeo.2016.12.005

[39] M. Brocchini, J. Calantoni, A. H. Reed, M. Postacchini, C. Lorenzoni, A. Russo, A. Mancinelli, S. Corvaro, G. Moriconi, L. Soldini, Summertime conditions of a muddy estuarine environment: the EsCoSed project contribution, Water Science and Technology 71 (10) (2015) 1451–1457. doi:10.2166/wst.2015.116.
URL https://doi.org/10.2166/wst.2015.116

[40] A. Valle-Levinson (Ed.), Contemporary Issues in Estuarine Physics, Cambridge University Press, 2010. doi:10.1017/CBO9780511676567.
URL https://doi.org/10.1017/CBO9780511676567

[41] M. Postacchini, L. Soldini, C. Lorenzoni, A. Mancinelli, Medium-term dynamics of a middle Adriatic barred beach, Ocean Science 13 (5) (2017) 719–734. doi:10.5194/os-13-719-2017.
URL https://doi.org/10.5194/os-13-719-2017

[42] L. Melito, M. Postacchini, A. Sheremet, J. Calantoni, G. Zitti, G. Darvini, M. Brocchini, Wave-current interactions and infragravity wave propagation at a microtidal inlet, Proceedings 2 (11) (2018) 628. doi:10.3390/proceedings2110628.

[43] R. G. Dean, R. A. Dalrymple, Water Wave Mechanics for Engineers and Scientists, World Scientific, 1991. doi:10.1142/1232.

[44] S. Elgar, T. H. C. Herbers, M. Okihiro, J. Oltman-Shay, R. T. Guza, Observations of infragravity waves, Journal of Geophysical Research 97 (C10) (1992) 15573–15577. doi:10.1029/92jc01316.
URL https://doi.org/10.1029/92JC01316

[45] J. A. Battjes, H. J. Bakkenes, T. T. Janssen, A. R. van Dongeren, Shoaling of subharmonic gravity waves, Journal of Geophysical Research 109 (C2). doi:10.1029/2003jc001863.

[46] R. T. Guza, E. B. Thornton, Observations of surf beat, Journal of Geophysical Research 90 (C2) (1985) 3161. doi:10.1029/jc090ic02p03161.

[47] J. M. Smith, H. E. Bermudez, B. A. Ebersole, Modeling waves at Willapa Bay, Washington, in: Coastal Engineering 2000, American Society of Civil Engineers, 2001. doi:10.1061/40549(276)64.

[48] K. Kang, D. Di Iorio, Depth- and current-induced effects on wave propagation into the Altamaha River Estuary, Georgia, Estuarine, Coastal and Shelf Science 66 (3-4) (2006) 395–408. doi:10.1016/j.ecss.2005.09.008.